



Co₄S₃ grafted 1 T-phase dominated WS₂ ultrathin nanosheet arrays for highly efficient overall water splitting in alkaline media

Qimin Peng^a, Xue Shao^a, Chuan Hu^a, Zuyang Luo^a, Tayirjan Taylor Isimjan^{c,*}, Zhifeng Dou^{b,*}, Ruobing Hou^a, Xiulin Yang^{a,*}

^aGuangxi Key Laboratory of Low Carbon Energy Materials, School of Chemistry and Pharmaceutical Sciences, Guangxi Normal University, Guilin, Guangxi 541004, China

^bState Key Laboratory of Advanced Materials of Tropical Island Resources (Ministry of Education), Hainan University, Haikou, Hainan 570228, China

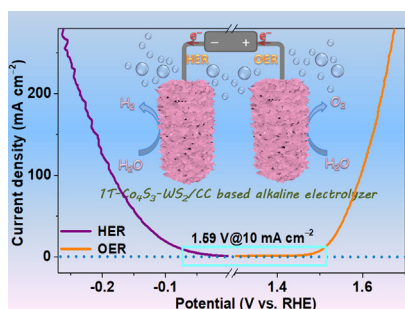
^cSaudi Arabia Basic Industries Corporation (SABIC) at King Abdullah University of Science and Technology (KAUST), Thuwal 23955-6900, Saudi Arabia

HIGHLIGHTS

- 1 T-Co₄S₃-WS₂/CC is constructed by *in-situ* growth and vulcanization strategies.
- The catalyst displays a remarkable OER/HER activity of 278 mV/75 mV@10 mA cm⁻².
- The bifunctional catalyst only requires 1.59 V cell voltage to reach 10 mA cm⁻² in overall water splitting.
- The synergy between Co₄S₃ and 1 T-WS₂ contributes to improving water splitting kinetics.

GRAPHICAL ABSTRACT

A highly effective 1T-Co₄S₃-WS₂ ultrathin nanosheet arrays on carbon cloth is successfully constructed by a facile *in-situ* growth and vulcanization strategies. Electrochemical studies illustrated that the designed bifunctional catalyst exhibited excellent OER/HER catalytic, long-term stability, as well as the simulated two electrode system.



ARTICLE INFO

Article history:

Received 13 November 2021

Revised 14 January 2022

Accepted 7 February 2022

Available online 8 February 2022

Keywords:

1T-Co₄S₃-WS₂

Ultrathin nanosheet arrays

Synergistic effect

Oxygen and hydrogen evolution

Overall water splitting

ABSTRACT

Developing the earth-abundant transition metal-based bifunctional electrocatalysts for water splitting and renewable energy devices has attracted much attention. Herein, we report a 1 T-WS₂ in ultrathin nanosheet arrays grafted with Co₄S₃ on conductive carbon cloth (CC) (1 T-Co₄S₃-WS₂/CC) through a feasible *in-situ* growth and vulcanization. The optimized 1 T-Co₄S₃-WS₂/CC catalyst exhibits an impressive electrocatalytic activity and remarkable stability with the oxygen/hydrogen evolution reaction (OER/HER): 278/75 mV for 10 mA cm⁻²). It also showed the small Tafel slope values of 61.7 and 58.4 mV dec⁻¹, respectively. Additionally, the 1 T-Co₄S₃-WS₂/CC^(-/+) achieved 1.59 V@10 mA cm⁻² in alkaline media superior to the most previously reported non-precious metal electrocatalysts. The outstanding performance could be attributed to the synergy between heterostructures of Co₄S₃ and 1 T-WS₂ modifying the electronic structure to accelerate water splitting kinetics. Thus, this work presents a rational design of scalable, high-efficiency, stable water splitting electrocatalysts based on WS₂.

© 2022 Elsevier Inc. All rights reserved.

1. Introduction

Developing efficient and sustainable clean energy technologies has become an urgent concern for the scientific community [1–

* Corresponding authors.

E-mail addresses: isimjant@sabic.com (T. Taylor Isimjan), douzf@hainanu.edu.cn (Z. Dou), xlyang@gxnu.edu.cn (X. Yang).

3]. Hydrogen production through electrochemical water splitting is considered a viable approach to resolving the energy crisis and environmental problems, which has aroused extensive attention recently due to the high energy density and pollution-free feature [4,5]. Unfortunately, the anodic oxygen evolution reaction (OER) and cathodic hydrogen evolution reaction (HER) require large overpotentials. Significantly, the OER catalysts demand high overpotentials for overcoming the kinetically slow multi-electron transfer process [6–9]. The high overpotential can be lowered by constructing a unique structure-function relationship to elucidate more active sites [10] and creating a positive synergy between various compositions in the catalysts [11].

The precious-metal-based electrocatalysts, such as Ru-, Ir- and Pt, and their oxides are recognized as the most suitable OER and HER catalysts regardless of their scarcity and high cost, which primarily hinders the widespread commercialization [12]. Therefore, considerable efforts have been devoted to exploring earth-abundant and stable non-noble-metal electrocatalysts, including metal chalcogenides, carbides, and phosphides [11,13–15]. Furthermore, bifunctionality permits an additional cost reduction and better stability at a higher operating voltage range, thereby extending the catalyst's lifetime during the regeneration through bias-switching. Recently, the transition metal chalcogenides (TMCs) such as MoS₂ [16], CoS₂ [17], NiS₂ [18], WS₂ [19] have been widely investigated due to their abundance, high electronic conductivity, and good chemical stability [20,21].

Notably, the WS₂ is considered as promising HER electrocatalyst owing to its multiple oxidation states, superior chemical stability, and high melting point. The WS₂ is formed of multilayered nanosheet arrays that produce polymorphism with distinctive phases like 1 T (metallic), 2H, and 3R (semiconductor) [22,23]. Moreover, density functional theory (DFT) studies have shown that the 1 T-WS₂ exhibits excellent HER performance in alkaline media, thanks to the lower bandgap and high base surface active sites [24]. Yet some properties of 1 T-WS₂ significantly hamper its further application in electrocatalysis [25], including (1) The lower density and reactivity of active sites. (2) The limited corrosion stability in an acid medium. (3) The poor thermodynamic stability and scalability. Moreover, the electrocatalytic behavior of 1 T-WS₂ to OER has not been investigated thoroughly. Specifically, combining the 1 T-WS₂ with other sulfides showed better performance through high conductivity and synergy between the components [26]. Apart from the synergetic effect, designing the high specific surface area porous catalysts to expose the active sites is critical for improving water splitting performance [27]. Therefore, we decide to develop an electrocatalyst with unique synergy between the compounds that complement each other positively and a structure-function relationship, which elucidates more active sites [28].

Herein, we proposed a rational design of the ultrathin nanosheet arrays structure of 1 T-Co₄S₃-WS₂/CC for OER and HER catalysis in alkaline environments. The achieved 1 T-Co₄S₃-WS₂/CC shows good activity and remarkable durability against OER and HER. The overpotential of OER at 10 mA cm⁻² is as low as 278 mV, and the Tafel slope is 61.7 mV dec⁻¹. For HER, it has a Tafel slope of 58.4 mV dec⁻¹, and an ultra-low overpotential (75 mV@10 mA cm⁻²). Besides, the 1 T-Co₄S₃-WS₂/CC^(-/+) two-electrode system requires a cell voltage of 1.59 V to reach 10 mA cm⁻² and shows outstanding long-term durability for at least 100 h with almost no degradation, illustrating an excellent economic perspective for large-scale H₂ production. The detailed characterizations revealed unusual activity results from a strong coupling effect with heterogeneous structure between Co₄S₃ and 1 T-WS₂, good electronic conductivity, and accessible active sites.

2. Experimental section

2.1. Materials and chemicals

Cobalt chloride hexahydrate (CoCl₂·6H₂O, 99.5%, Aladdin, 500 g), ammonium metatungstate ((NH₄)₆H₂W₁₂O₄₀·xH₂O, 99.5%, Aladdin, 100 g), polymer F127 (MW = 12600, Aladdin, 1 kg), sulfur powder (S, 99.5%, Xilong, 500 g), potassium hydroxide (KOH, 90%, Macklin, 500 g), ethanol (C₂H₅OH, 99.7%, Xilong, 500 mL), hydrochloric acid (HCl, 37%, Xilong, 500 mL), commercial Pt/C (20 wt% Pt, Sinero, 1 g), carbon cloth (CC, WOS1009, 0.33 × 400 × 400 mm). RuO₂ powder was prepared by directly annealing RuCl₃·3H₂O (37%, Inno-chem, 25 g) at 400 °C in air. All chemical reagents were used directly without further purification.

2.2. Synthesis of Co₄W₆O₂₁(OH)₂·4H₂O on CC (CoWO/CC)

Typically, the CC (2 × 3 cm) was successively cleaned by 0.5 M HCl, deionized water, and ethanol in an ultrasonication unit for 15 min. A mixture of 1.5 mmol CoCl₂·6H₂O, 0.1 mmol (NH₄)₆H₂W₁₂O₄₀·xH₂O and 200 mg polymer F127 were dissolved in deionized water (20 mL), which was continuously stirred for 30 min to form a homogeneous solution, then transferred into a Teflon-lined stainless steel autoclave (50 mL) with a pre-treated CC in it. The autoclave was heated at 200 °C for 6 h and then cooled down to room temperature. The obtained product (named as CoWO/CC) was taken out and rinsed with deionized water and dried under vacuum at 60 °C.

2.3. Synthesis of 1 T-Co₄S₃-WS₂ on CC (1 T-Co₄S₃-WS₂/CC)

The obtained CoWO/CC and 0.5 g sulfur powders were put at the center and upstream side of the tube furnace, respectively. The furnace was heated up to 400, 500, and 600 °C at a ramping rate of 5 °C min⁻¹ and annealed for 2 h under N₂ atmosphere. After naturally cooling to room temperature, the obtained samples were marked as 1 T-Co₄S₃-WS₂/CC-400, -500, and -600, separately. The loading of 1 T-Co₄S₃-WS₂ on CC is approximately 3.3 mg cm⁻². Furthermore, we prepared two groups of 1 T-Co₄S₃-WS₂/CC-500 catalysts, calcined with different mass ratios of S powder (2:1 and 1:2), and compared the electrocatalytic performance. The Co₄S₃/CC and WS₂/CC were synthesized according to the methods reported in the previous literature [25,29,30].

2.4. Material characterizations

Morphologies and microstructures of samples were characterized by scanning electron microscopy (SEM, FEI Quanta 200) and transmission electron microscopy (TEM, JEM-2100F). The crystallography of the catalyst was investigated by X-ray powder diffraction (XRD, Rigaku D/Max 2500 V/PC) with Cu K α radiation. The elements and chemical valence of catalysts were detected by X-ray photoelectron spectroscopy (XPS, JPS-9010TR, Japan). Brunauer-Emmett-Teller (BET) surface area and pore size distribution of materials were analyzed by a Quantachrome instrument (3H-2000PS4). Raman spectra of catalysts were conducted at a Raman instrument (Renishaw inVia) with a 514 nm excitation laser. The thickness of the sample was analyzed by Atomic Force Microscopy (AFM) on a Bruker (Dimension ICON) scanning probe microscope. The actual metal loadings in the samples were measured by inductively coupled plasma atomic emission spectrometry (ICP-AES, IRIS Intrepid II XSP).

2.5. Electrochemical measurements

All electrochemical tests were performed on a Biologic VMP3 electrochemical workstation with a standard three-electrode system in a 1.0 M KOH (pH \approx 13.5) electrolyte. The catalysts electrode ($1 \times 1 \text{ cm}^2$), graphite plate, and standard calomel electrodes (SCE) were applied as the working, counter, and reference electrodes, respectively. Cyclic voltammetry (CV) tests at a scan rate of 10 mV s^{-1} were used to stabilize the catalysts' performance. The electrochemical double-layer capacitance (C_{dl}) of the electrocatalysts were obtained by CV at different scan rates, and the equation calculated the C_{dl} : $C_{dl} = (j_a - j_c) / (2 \times \nu)$. Where j_a , j_c , and ν correspond to the current density of anode and cathode and the scan rate, respectively. The C_{dl} was used to estimate the electrochemical active surface area (ECSA). Linear sweep voltammetry (LSV) was conducted on a scan rate of 1 mV s^{-1} . Electrochemical impedance spectroscopy (EIS) measurements were carried out near the onset potential with the frequency range from 200 kHz to 10 MHz. All potentials (vs. SCE) were calibrated by the equation: $E_{RHE} = E_{SCE} + 0.242 + 0.059 \times \text{pH}$ (Fig. S1). The overall water splitting test was implemented in a two-electrode system with the voltage range of 0–2.0 V (vs. SCE) at a scan rate of 5 mV s^{-1} in 1.0 M KOH electrolyte, and all reported curves were corrected against iR compensation.

3. Results and discussion

3.1. Synthesis and structural analysis

The synthesis procedure of 1 T-Co₄S₃-WS₂/CC was schematically illustrated in Fig. 1a. The interlinked nanowires grown on CC were initially prepared by a facile hydrothermal reaction at 200 °C for 6 h, and the corresponding crystal structure was determined as cubic Co₄W₆O₂₁(OH)₂·4H₂O (JCPDS: 47-0142) by X-ray powder diffraction (XRD) (Fig. S2a) [31]. Afterward, the as-prepared CoWO/CC was treated with 0.5 g sulfur powders at different temperatures of 400, 500, and 600 °C for 2 h under N₂ flowing to synthesize 1 T-Co₄S₃-WS₂/CC. As shown in Fig. 1b, after vulcanization treatment, the crystal structure of the catalyst has changed, the representative six diffraction peaks at 14.4°, 33.5°, 41.2°, 44.4°, 58.7°, and 60.5° are designated for the (003), (101), (015), (009), (110), and (1010) lattice planes of hexagonal 1 T-WS₂ (JCPDS: 35-0651) [25,32], respectively. Meanwhile, the other diffraction peaks located at 30.0°, 50.0°, and 73.4° are identified as the planes (111),

(220), and (400) of cubic Co₄S₃ phase (JCPDS: 30-0458) [33]. The broad peak around 26° belongs to graphitic carbon's (002) lattice plane. Significantly, when the vulcanization temperature is 400 °C, the crystal structure of the catalyst is consistent with CoWO (Figs. S2b-c), indicating that lower temperature cannot successfully convert the material into sulfide. Moreover, the vulcanized catalyst's BET and ECSA at 600 °C were lower than those of the vulcanization product at 500 °C. It suggests the collapsing of porous morphology above 500 °C, thereby lowering electrocatalytic performance. As a result, the optimal performance was achieved after vulcanization at 500 °C.

Raman spectroscopy further analyzes the catalysts' crystal form, phase state, and crystallinity changes during the process. As displayed in Fig. 1c and Fig. S3, the characteristic Raman modes at 352.3 and 415.0 cm⁻¹ are ascribed to the plane E_{2g}¹ and A_{1g} vibration modes, demonstrating the formation of 2H phase WS₂ [20,34]. In addition, due to the small content of Co₄S₃ in WS₂, four relatively immature Raman modes at 140, 175, 230, and 325 cm⁻¹ in the low-frequency region are attributed to J₁, J₂, A_g, and J₃ peaks, respectively, clearly confirming the formation of 1 T phase WS₂ [24,34]. However, The Raman peak intensity does not reflect the actual content of the specific crystal phase. XPS is used to determine the 2H and 1 T phases composition of WS₂ [35]. The XPS spectrum indicated that the content of 1 T-WS₂ is much higher than that of 2H-WS₂.

Since the preliminary analysis showed that 1 T-Co₄S₃-WS₂/CC-500 electrocatalyst is provided with better catalytic performance, the Brunauer-Emmett-Teller (BET) gas adsorption test was carried out on its surface properties. The N₂ adsorption-desorption isotherm curve of 1 T-Co₄S₃-WS₂/CC-500 illustrated the BET surface area of 58.0 m² g⁻¹ and was confirmed as the typical type iii isotherm. Moreover, the 1 T-Co₄S₃-WS₂/CC-500 electrocatalyst exhibits a particle size of 24.8 nm and a pore volume of 0.30 cm³ g⁻¹ [36], which are significantly higher than 1 T-Co₄S₃-WS₂/CC-(400, 600) (Fig. 1d and Fig. S4). The presence of mesopores structure with a high BET surface area in the 1 T-Co₄S₃-WS₂/CC-500 can enhance the electrolyte mobility toward the OER/HER active sites, therefore reducing transfer resistance [37].

The morphology and microstructure of the 1 T-Co₄S₃-WS₂/CC-500 were characterized by scanning electron microscope (SEM) and transmission electron microscope (TEM). Fig. S5a shows that the surface of the cleaned CC was smooth. The precursor CoWO/CC presents a cross-linked nanowires structure at high magnification (Fig. 2a), which appears as a spherical structure consisting of many nanowires under low-magnification SEM images (Figs. S5b-

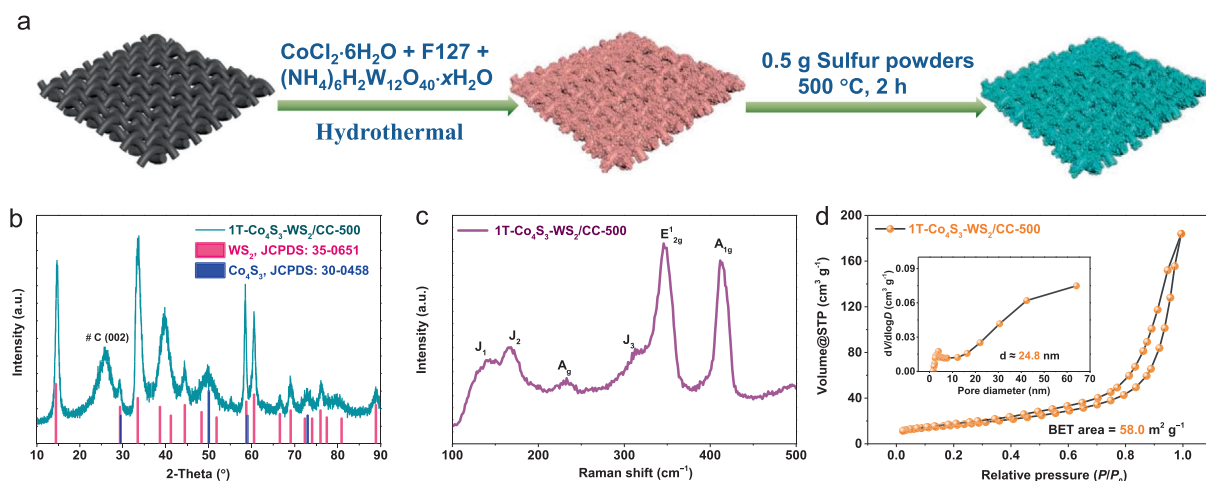


Fig. 1. (a) Schematic representation of the 1 T-Co₄S₃-WS₂/CC-500 catalyst synthesis procedure. (b) XRD pattern, (c) Raman spectrum, and (d) N₂ adsorption-desorption isotherm with BJH pore-size distribution curve of 1 T-Co₄S₃-WS₂/CC-500.

c), indicating a high level of porosity. Upon vulcanization, the 1 T-Co₄S₃-WS₂/CC-500 catalyst morphology is transformed from nanowires to nanosheets (Fig. 2b). Notably, the morphology of 1 T-Co₄S₃-WS₂/CC-400 is similar to CoWO/CC, consistent with the XRD results (Figs. S2b–c). Furthermore, when changing the amount of (NH₄)₆H₂W₁₂O₄₀·xH₂O (0.05 and 0.15 mmol), the morphology of the catalyst does not change significantly (Fig. S6), showing the minor impact of the precursor concentration towards the surface morphology. Additionally, the TEM image of 1 T-Co₄S₃-WS₂/CC-500 (Fig. 2c) was obtained and once again confirmed the nanosheet arrays structure. The high-resolution TEM (HRTEM) image displayed a series of lattice fringes of 0.157, 0.267, 0.324, 0.182 nm, and 0.337 nm corresponding to the (110), (101), and (006) crystal planes of 1 T-WS₂, and (220) crystal plane of Co₄S₃, and (002) crystal plane of graphite carbon, respectively (Fig. 2d) [38]. As shown in Fig. 2e–f, the nanosheet arrays consist of ultrasmall crystalline nanodomains (labeled regions 1 and 2) as the main component. The selected area electron diffraction (SAED) pattern also reaffirmed the existence of (101), (220), and (110) crystal planes for 1 T-Co₄S₃-WS₂/CC-500 and further revealed a polycrystalline structure of the 1 T-Co₄S₃-WS₂/CC-500 nanosheet arrays (Fig. 2g) [39]. The energy dispersive X-ray (EDX) pattern (Fig. 2h) proved the coexistence of Co, W, S, and C elements. Atomic force microscopy (AFM) verified the morphology of 1 T-Co₄S₃-WS₂/CC-500 nanosheet arrays and indicated that the thickness of nanosheet

arrays was 2.2 nm (Fig. 2i–j). Moreover, the EDS elemental mapping images showed the homogeneous distribution of C, Co, W, and S elements within the 1 T-Co₄S₃-WS₂/CC-500 nanosheet arrays (Fig. 2k–n). The inductively coupled plasma atomic emission spectrometry (ICP-AES) test revealed that 1 T-Co₄S₃-WS₂/CC-500 catalyst is composed of Co (5.73 wt%) and W (73.92 wt%) (Table S1). The ICP results further support the XRD analysis to prove the successful formation of 1 T-Co₄S₃-WS₂/CC.

3.2. X-ray photoelectron spectroscopy

The X-ray photoelectron spectroscopy (XPS) measurement is performed to explore the valence state and composition of the sample. The full survey spectrum further confirmed the existence of Co, C, S, and W elements in 1 T-Co₄S₃-WS₂/CC (Fig. S7a). For 1 T-Co₄S₃-WS₂/CC-500, the C 1s spectrum can be deconvoluted into three peaks at binding energies of 284.8, 286.0, and 289.1 eV, which are attributed to C–C, C–O, and C=O bonds, respectively (Figs. S7b–d) [40,41]. In Fig. 3a, the Co 2p XPS spectrum shows six peaks, analogously, two characteristic peaks at 779.3 and 794.3 eV are ascribed to Co³⁺ in Co₄S₃, while two peaks at 781.9 and 797.9 eV corresponding to the Co²⁺ 2p_{3/2} and 2p_{1/2}, respectively, and the other two shakeup satellite peaks at 785.5 and 802.3 eV [33,42]. Meanwhile, the XPS peak belonging to Co³⁺ in Co₄S₃/CC illustrates a positive shift (0.8 eV) compared to 1 T-

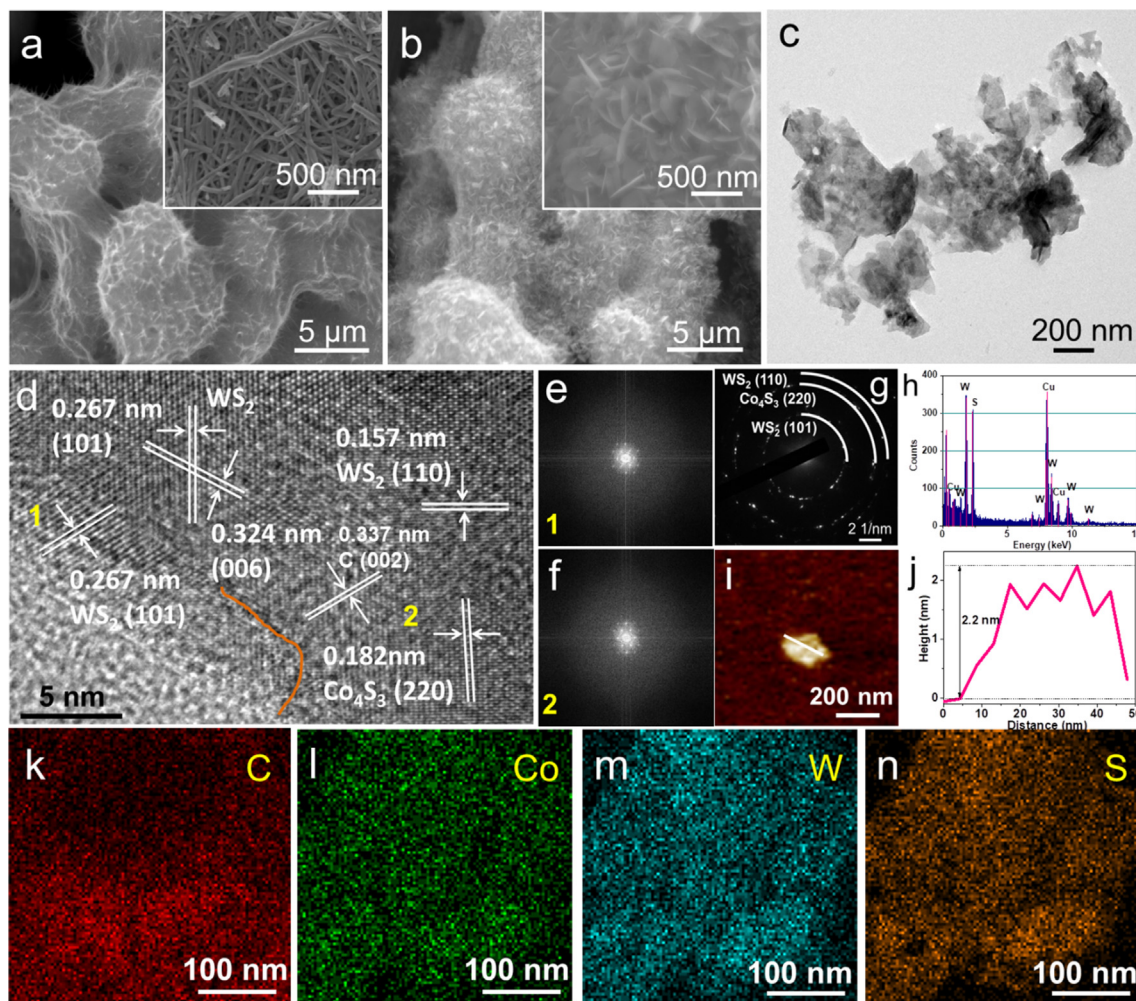


Fig. 2. SEM images of (a) CoWO/CC and (b) 1 T-Co₄S₃-WS₂/CC-500. (c) TEM image, (d) high-resolution TEM image, and (e–f) FFT diffraction patterns for the marked regions 1 and 2 in a panel of 1 T-Co₄S₃-WS₂. (g) SAED pattern, (h) EDX spectrum, (i–j) AFM image and the corresponding height profiles, and (k–n) EDS elemental mapping images of 1 T-Co₄S₃-WS₂/CC-500 nanosheet arrays.

Co₄S₃-WS₂/CC, revealing that more electrons can be transferred from Co to W in the catalyst [43,44]. In addition, in the XPS spectrum of W 4f (Fig. 3b), the main binding energy peaks at 32.0 eV (W⁴⁺ 4f_{7/2}) and 34.2 eV (W⁴⁺ 4f_{5/2}) corresponding to the 1 T-phase, whereas two peaks at 32.7 and 34.8 eV are assigned to the 2H-phase of WS₂ as stated in the previous research report [35,45]. The other two peaks are ascribed to W – O bonds, the existence of W – O is inevitable due to the surface oxidation of WS₂ [20,34]. Compared with the 2H-phase, the peak intensity of the 1 T-phase is much stronger, which indicates that the 1 T-phase dominated ultrathin nanosheet arrays structure of 1 T-Co₄S₃-WS₂/CC. Interestingly, careful study of the W 4f XPS shows that the binding energies for W 4f_{7/2} in 1 T-WS₂/CC exhibit a negative shift (0.5 eV) compared with 1 T-Co₄S₃-WS₂/CC. The above results indicate the presence of partial electron transfer from Co to W in 1 T-Co₄S₃-WS₂/CC, which results from the strong electronic coupling effect among Co and W [44]. And the oxygen XPS profile (Fig. S8) was deconvoluted into three peaks at 529.9, 531.1, and 533.3 eV, which can be indexed to metal-oxygen (M – O), carbon-oxygen (C – O), and adsorbed OH groups (O_A) [5,46], respectively. Meanwhile, as presented in Fig. 3c, the S 2p region is deconvoluted into four peaks at 162.5 eV (S 2p_{3/2}) and 163.6 eV (S 2p_{1/2}), which correspond to metal-S [30,47]. Overall, as expected, the XPS analysis further determined that the 1 T-Co₄S₃-WS₂ was successfully prepared, which is well-aligned with the XRD and TEM results.

3.3. Electrocatalytic OER analysis

The OER performance of 1 T-Co₄S₃-WS₂/CC was measured by a standard three-electrode system in 1.0 M KOH. The 1 T-Co₄S₃-WS₂/CC-500 catalyst only needs 278, 328, and 366 mV to drive 10, 50, and 100 mA cm⁻², respectively (Fig. 4a-b), the 1 T-Co₄S₃-WS₂/CC-500 catalyst possesses the highest electrocatalytic OER activity as compared to its counterpart. In Fig. 4c, the corresponding Tafel slope of 1 T-Co₄S₃-WS₂/CC-500 (61.7 mV dec⁻¹) is smaller than

those of CoWO (72.5 mV dec⁻¹), 1 T-Co₄S₃-WS₂/CC-400 (69.3 mV dec⁻¹), and 1 T-Co₄S₃-WS₂/CC-600 (67.4 mV dec⁻¹), even comparable to RuO₂/CC (61.1 mV dec⁻¹), indicating the 1 T-Co₄S₃-WS₂/CC-500 catalyst exhibit enhanced kinetics for OER [48]. It is worth noting that the 1 T-Co₄S₃-WS₂/CC-500 catalyst shows comparable and even better OER activity than some advanced catalysts reported so far (Fig. 4d and Table S2). Also, we studied the effect of different amounts of (NH₄)₆H₂W₁₂O₄₀·xH₂O (0.05 and 0.15 mmol) toward the OER catalytic performance of 1 T-Co₄S₃-WS₂/CC (Fig. S9). Herein, the OER performance of 1 T-Co₄S₃-WS₂/CC-500 was investigated in acidic (0.5 M H₂SO₄) and neutral solution (1.0 M PBS); they both showed inferior performances (Figs. S10–11). To explore the possible reason for the high activity of the 1 T-Co₄S₃-WS₂/CC-500 catalyst, we first investigate the electrochemical active surface area (ECSA) of the catalysts based on the double-layer capacitance (C_{dl}). The C_{dl} of different catalysts is obtained from the CV curves at multiple scan rates in non-Faradaic regions (Figs. S12–13). Meanwhile, the C_{dl} value of 1 T-Co₄S₃-WS₂/CC-500 is 214.8 mF cm⁻² (Fig. 4e), which is much larger than all control catalysts (Table 1). Besides, the ECSA has been calculated by the equation (1):

$$ECSA = C_{dl}/C_s \quad (1)$$

The catalyst's electrochemical active surface area (ECSA) is directly proportional to the number of active sites. The C_s is usually in the range of 20–60 μF cm⁻² to calculate the ECSA value in 1.0 M KOH solution, and the average value of C_s (40 μF cm⁻²) used in this work [49,50]. The results show that the 1 T-Co₄S₃-WS₂/CC-500 catalyst retains the maximum ECSA of 3580 cm² higher than those of CoWO (1168 cm²), 1 T-Co₄S₃-WS₂/CC-400 (2438 cm²), and 1 T-Co₄S₃-WS₂/CC-600 (3058 cm²) (Fig. 4f). The largest ECSA value provides more catalytic active sites for OER. Furthermore, the superior catalytic performance of 1 T-Co₄S₃-WS₂/CC-500 catalyst also benefits from the abundant reaction sites and ultrathin nanosheet arrays structure with high specific surface area. To understand the intrinsic activity of each active site, the LSV curves using

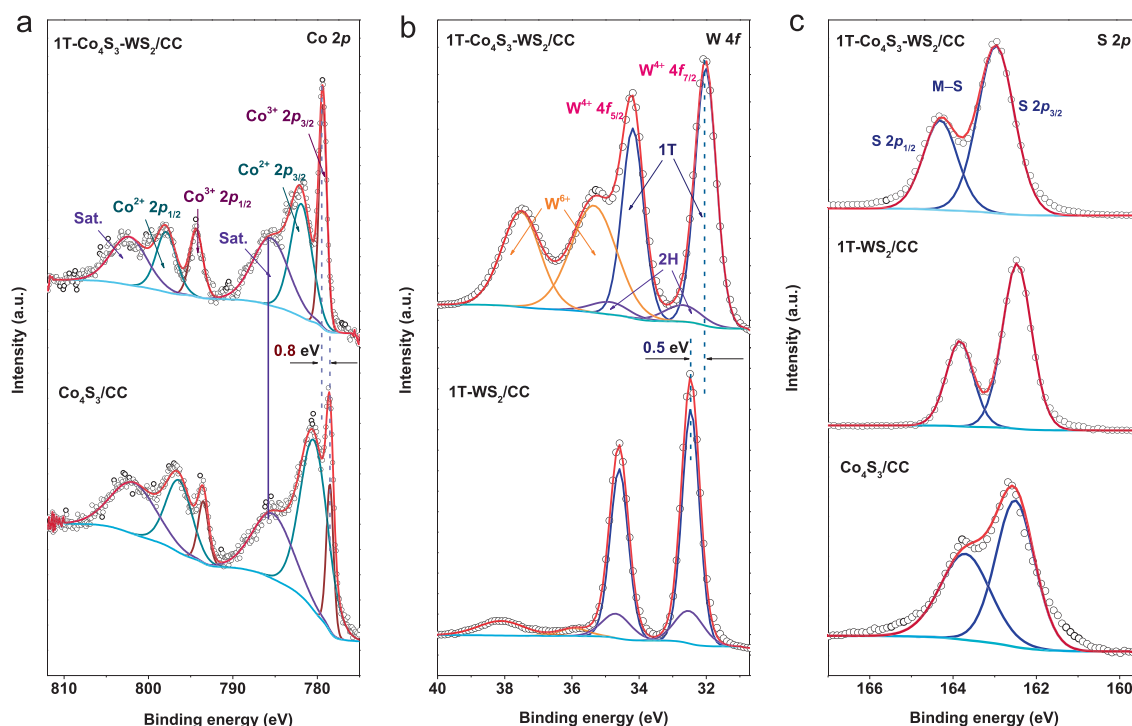


Fig. 3. The high resolution XPS spectra of (a) Co 2p, (b) W 4f, and (c) S 2p of 1 T-Co₄S₃-WS₂/CC, Co₄S₃/CC, and 1 T-WS₂/CC.

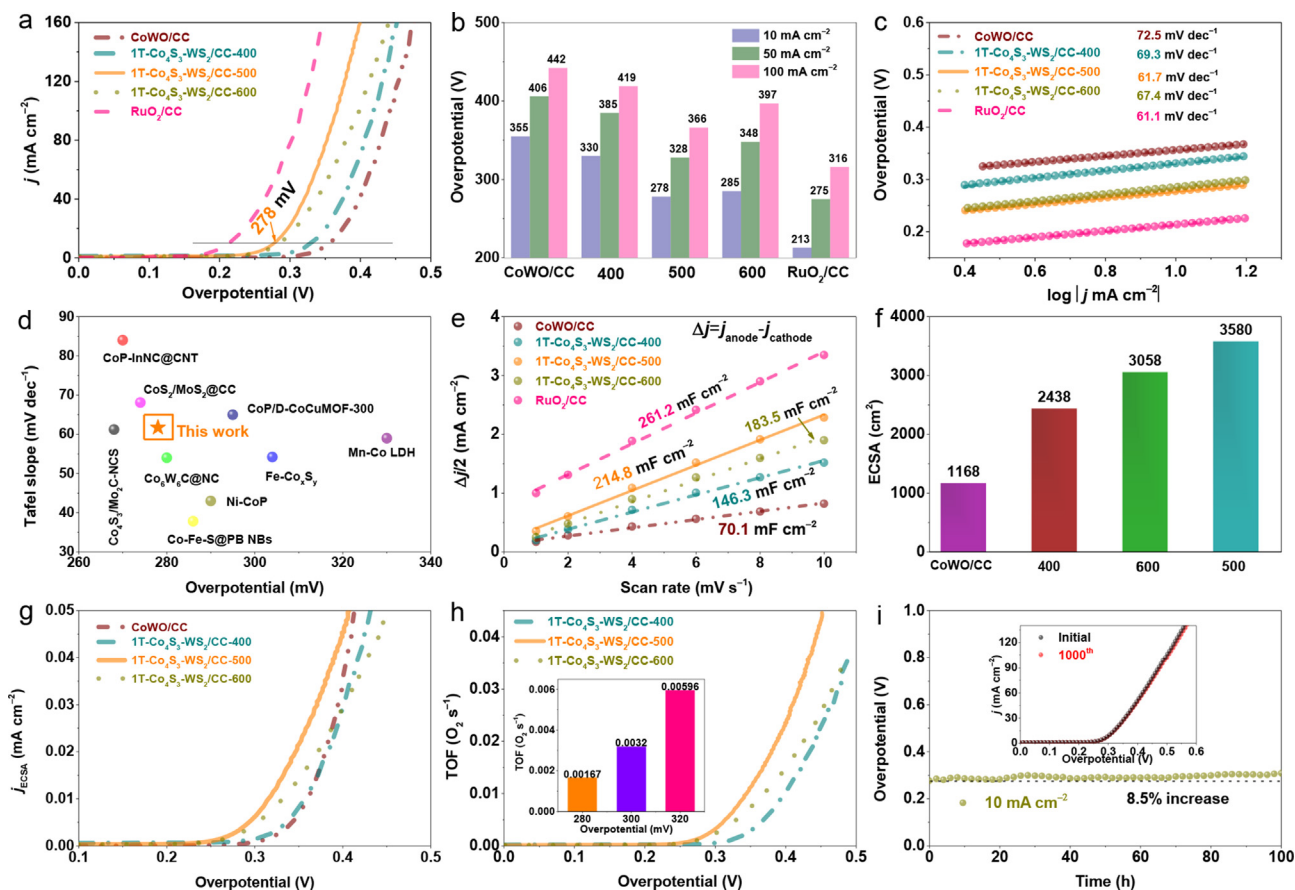


Fig. 4. Electrochemical OER performance in 1.0 M KOH. (a) LSV curves. (b) Comparison of overpotentials at 10, 50, and 100 mA cm⁻² for 1 T-Co₄S₃-WS₂/CC-500 and other samples. (c) Tafel slopes. (d) Overpotentials at 10 mA cm⁻² and Tafel slopes of some previously reported catalysts. (e) Double-layer capacitance (C_{dl}) plots. (f) Comparison of the ECSA of CoWO/CC, 1 T-Co₄S₃-WS₂/CC-(400, 500, and 600). (g) ECSA-normalized LSV curves. (h) Potential-dependent TOF curves (insert: the summarized TOF of 1 T-Co₄S₃-WS₂/CC-500 at applied overpotentials of 280, 300, and 320 mV). (i) Chronopotentiometry curve of 1 T-Co₄S₃-WS₂/CC-500 (insert: LSV curves initial and after 1000 CV cycles).

ECSA-normalized current density (j_{ECSA}) demonstrate the 1 T-Co₄S₃-WS₂/CC-500 has the highest intrinsic catalytic activity among all electrocatalysts (Fig. 4g). The turnover frequency (TOF) was calculated by ICP and was used to evaluate further the inherent activity of electrocatalysts Eq. (2):

$$TOF = \frac{j \times A}{4Fn} \quad (2)$$

where j is the current density, A is the electrode area with moles of catalyst, F is the Faraday constant (96485C mol⁻¹), and n is the number of active sites of all metals present in the electrode [51]. As shown in Fig. 4h, the TOF value of 1 T-Co₄S₃-WS₂/CC-500 increased more rapidly compared to 1 T-Co₄S₃-WS₂/CC-400 and 1 T-Co₄S₃-WS₂/CC-600 when the applied potential increases. The TOF values of the 1 T-Co₄S₃-WS₂/CC-500 catalyst are 0.00167, 0.0032, and 0.00596 s⁻¹ at overpotentials of 280, 300, and 300 mV. The higher TOF value indicates excellent OER intrinsic electrocatalytic activity.

Table 1

The summarized OER catalytic parameters of different catalysts in 1.0 M KOH solution.

Catalysts	η_{10} (mV)	Tafel slope (mV dec ⁻¹)	C_{dl} (mF cm ⁻²)	R_{ct} (Ω)
CoWO/CC	355	72.5	70.1	11.0
1 T-Co ₄ S ₃ -WS ₂ /CC-400	330	69.3	146.3	4.7
1 T-Co ₄ S ₃ -WS ₂ /CC-500	278	61.7	214.8	1.2
1 T-Co ₄ S ₃ -WS ₂ /CC-600	285	67.4	183.5	1.7
RuO ₂ /CC	213	61.1	261.2	0.6

Electrochemical impedance spectroscopy (EIS) measurement was implemented to investigate the charge transfer process between electrolyte and electrocatalyst. The Nyquist plots of the catalysts (Fig. S14a) manifest that the charge transfer resistance (R_{ct}) of 1 T-Co₄S₃-WS₂/CC-500 is smaller than CoWO 1 T-Co₄S₃-WS₂/CC-400, and -600, indicating the best conductivity and fast interface Faradaic reaction process. In addition, around 8.5% potential loss was detected during the chronopotentiometry measurement at 10 mA cm⁻² for 100 h on 1 T-Co₄S₃-WS₂/CC-500 (Fig. 4i). Meanwhile, an accelerated CV cycling test was conducted to investigate the catalytic robustness showing a negligible shift of polarization curves after cycling 1000 CVs (insert of Fig. 4i). The catalyst after the OER test was also subjected to XRD characterization. The result shows that the surface is composed of CoOOH and WO(O₂)-H₂O (Figure S21b). Further insights into the morphology of 1 T-Co₄S₃-WS₂/CC-500 after the OER stability test confirmed that the nanosheet arrays structure gradually collapses and agglomerates (Fig. S15a), and the change in the crystalline phase and the

morphology of the catalyst together to cause performance degradation.

3.4. Electrocatalytic HER analysis

Besides the exceptional OER activity, the distinguished HER performance was also achieved on the heterostructured 1 T-Co₄S₃-WS₂/CC-500 nanosheet arrays. As shown in Fig. 5a-b, the 1 T-Co₄S₃-WS₂/CC-500 catalyst displayed a relatively low overpotential of 75, 144, and 184 mV to yield 10, 50, and 100 mA cm⁻², surpassing the control catalysts. The electrocatalytic kinetics and mechanism were investigated by the Tafel slopes obtained by fitting the linear regions of Tafel plots. Obviously, the Tafel slope of 1 T-Co₄S₃-WS₂/CC-500 (58.4 mV dec⁻¹) was much lower than those of CoWO (102.6 mV dec⁻¹), 1 T-Co₄S₃-WS₂/CC-400 (98.9 mV dec⁻¹), 1 T-Co₄S₃-WS₂/CC-600 (79.2 mV dec⁻¹), and Pt/C/CC (65.5 mV dec⁻¹) (Fig. 5c). A small Tafel slope demonstrates rapid HER reaction kinetics on 1 T-Co₄S₃-WS₂/CC-500 and follows the Volmer–Heyrovsky mechanism. Meanwhile, the rate limit step is the electrochemical desorption of hydrogen [52,53]. Furthermore, the exchange current density (*j*₀) was calculated by extrapolating the Tafel slope, which is another key parameter reflecting the intrinsic activity of HER. As shown in Fig. 5d, the 1 T-Co₄S₃-WS₂/CC-500 exhibited higher value of 1.496 mA cm⁻² compared with CoWO (0.0123 mA cm⁻²), 1 T-Co₄S₃-WS₂/CC-400 (0.150 mA cm⁻²) and 1 T-Co₄S₃-WS₂/CC-600 (0.402 mA cm⁻²), the immense *j*₀ value of 1 T-Co₄S₃-WS₂/CC-500 represents the electrodes' faster electrochemical reaction rate at equilibrium. Meanwhile, the η_{10} and corresponding Tafel slope for 1 T-Co₄S₃-WS₂/CC-500 is lower than most of the HER electrocatalysts reported previously (Fig. 5e and Table S3). As shown in Fig. S14b, by order of HER performance, 1 T-Co₄S₃-WS₂/CC-500 delivers the lowest *R*_{ct} (4.5 Ω) among all control samples (Table 2), proving the rapid charge transfer at the interface of a heterostructure of 1 T-Co₄S₃-WS₂ and electrolyte, which is related to the better conductivity. In addition, we also discussed the effect of the amount of (NH₄)₆-H₂W₁₂O₄₀·*x*H₂O (0.05 and 0.15 mmol) on the HER performance of 1 T-Co₄S₃-WS₂/CC-500 (Fig. S16). At the same time, the HER activity of 1 T-Co₄S₃-WS₂/CC-500 was also tested in acidic (0.5 M

H₂SO₄) and neutral solution (1.0 M PBS), the 1 T-Co₄S₃-WS₂/CC-500 showed poor performance and was inferior to the alkaline condition (Figs. S10–11). The results showed that both catalysts' OER/HER performances were not as good as 1 T-Co₄S₃-WS₂, indicating the synergy between Co₄S₃ and WS₂ (Fig. S17). Furthermore, we optimized the performance of the 1 T-Co₄S₃-WS₂/CC-500 catalyst by changing the ratio of S powders (2:1, 1:1, and 1:2) used for sulfidation. The results showed that the catalyst exhibited the best OER and HER performance when the ratio of 1 T-Co₄S₃-WS₂/CC-500/S was 1:1 (Fig. S18).

For the stability, there is no apparent attenuation of the current densities of 10 and 100 mA cm⁻² over 70 h, demonstrating remarkable long-term stability for 1 T-Co₄S₃-WS₂/CC-500 (Fig. 5f). Meanwhile, the polarization curve shows an insignificant change after 1000 cycles CV in the potential range of 0 to -0.4 V (inset of Fig. 5f), indicating a potential for practical application. Interestingly, the nanosheet arrays structure after the HER stability test is well maintained, which could be one of the reasons for the excellent performance of HER (Fig. S15b). Besides, the XPS after the HER stability test is also unchanged (Figs. S19–20). On the other hand, the XPS full spectra after OER showed significant alterations. Notably, the ratio of Co³⁺/Co²⁺ increased, and the W⁶⁺ peak was fully converted into W⁴⁺ after the OER stability test indicating the importance of Co³⁺ for the OER performance. The disappearance of the W⁶⁺ improves the conductivity of the catalyst. The XRD characterization of the catalyst after the HER test showed that the crystal structure was transformed into Co(OH)₂ and WS₂, which proved that the transformation of Co₄S₃ to Co(OH)₂ after the HER test was beneficial to the HER process. The result of the XRD analysis showed that it was consistent with XPS (Fig. S21a).

3.5. Overall water splitting analysis

Based on the above analysis, 1 T-Co₄S₃-WS₂/CC-500 is a prominent candidate for efficient electrocatalytic water splitting. Inspired by OER and HER performance, a two-electrode configuration electrolyzer (1 T-Co₄S₃-WS₂/CC^(-/+)) was employed as an active catalyst (Fig. 6a). As plotted in Fig. 6b, the polarization curve shows that the 1 T-Co₄S₃-WS₂/CC^(-/+) electrolyzer delivers the

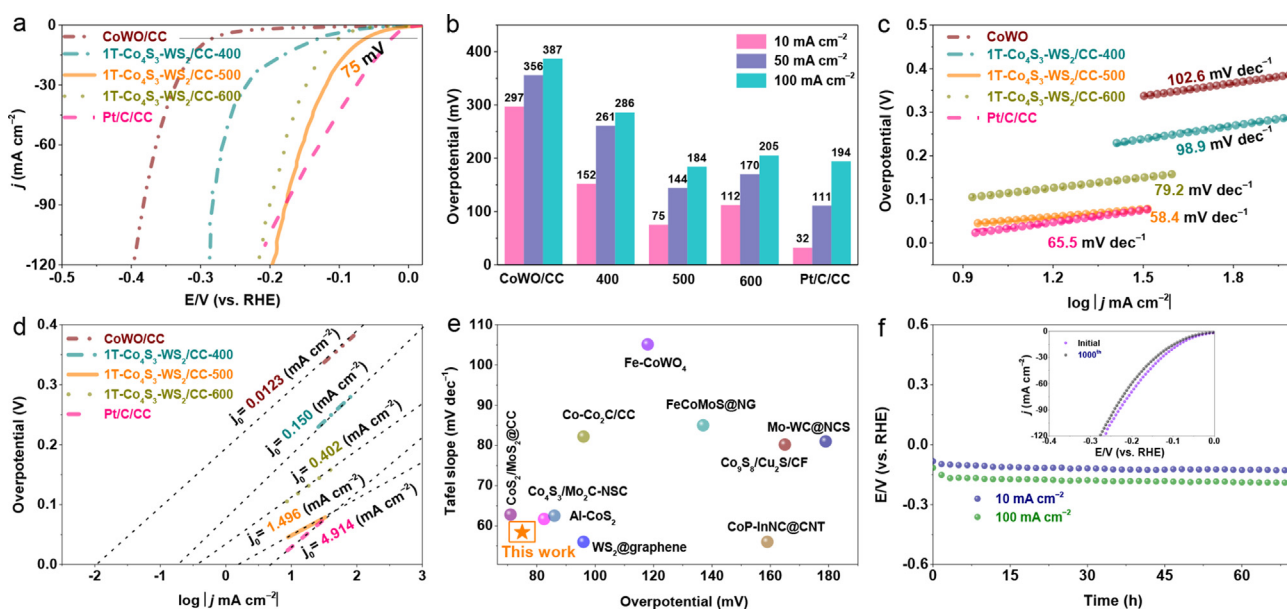


Fig. 5. Electrocatalytic HER performance in 1.0 M KOH. (a) LSV curves. (b) Comparison of overpotentials at 10, 50, and 100 mA cm⁻² for 1 T-Co₄S₃-WS₂/CC-500 and other samples. (c) Tafel slopes. (d) Exchange current density. (e) Comparison of the overpotentials at 10 mA cm⁻² and Tafel plots of 1 T-Co₄S₃-WS₂/CC-500 with recently reported catalysts. (f) Chronopotentiometry test at 10 and 100 mA cm⁻² (insert: LSV curves initial and after 1000 CV cycles).

Table 2

The summarized HER catalytic parameters of different catalysts in 1.0 M KOH solution.

Catalysts	η_{10} (mV)	Tafel slope (mV dec ⁻¹)	j_0 (mA cm ⁻²)	R_{ct} (Ω)
CoWO/CC	297	102.6	0.0123	194
1 T-Co ₄ S ₃ -WS ₂ /CC-400	152	98.9	0.150	18.4
1 T-Co ₄ S ₃ -WS ₂ /CC-500	75	58.4	1.496	4.5
1 T-Co ₄ S ₃ -WS ₂ /CC-600	112	79.2	0.402	8.9
Pt/C/CC	32	65.5	4.914	0.7

lower cell voltage of 1.59 V at 10 mA cm⁻². The alkaline electrolyzer outperformed the Pt/C(-)||RuO₂(+) benchmark when the current density was higher than 80 mA cm⁻². More importantly, it was evident from the long-term durability test that the 1 T-Co₄S₃-WS₂/CC(-/+) electrolyzer is stable for more than 100 h at 10 mA cm⁻² without substantial potential decay (Fig. 6c). It is comparable or even better than most reported electrocatalysts on the overall water splitting process (Fig. 6d and Table S4). The outstanding stability indicates a potential to develop high-activity 1 T-Co₄S₃-WS₂/CC catalysts for large-scale water splitting.

3.6. Catalytic mechanism analysis

As discussed above, the exceptional OER and HER electrocatalytic activity and durability, superior overall water splitting performance in the 1 T-Co₄S₃-WS₂/CC-500 catalyst can be attributed to the following aspects. (1) The nanosheet arrays catalyst has a large specific surface area and a mesoporous structure that accelerates the charge transfer and faster gas released during the reaction. (2) an immense ECSA value means more active sites that promote higher electrocatalytic OER, HER, and overall water splitting performance [54]. (3) Previous studies have shown that introducing

a suitable second component in the mixed catalyst can optimize the adsorption energy of the active sites. During the OER/HER process, a part of the Co₄S₃ and 1 T-WS₂ component surface was primarily oxidized to be Co/W oxide/hydroxide, which creates the contact between Co₄S₃ and 1 T-WS₂ components [55,56]. (4) In situ interface engineering design 1 T-Co₄S₃-WS₂/CC can generate a metal-sulfur bond, which increases the effective reaction sites of the active surface [57]. The strong metal-sulfur bond interaction increases the local electron state of the W atom, thus reducing the energy of proton to hydrogen, and improving the intrinsic activity of the catalyst, thereby synergistically enhancing the catalytic activity of the OER/HER process.

4. Conclusions

In summary, we developed a practical and straightforward approach to fabricate an ultrathin nanosheet arrays 1 T-Co₄S₃-WS₂ catalyst. Notably, the nanosheet arrays structure *in situ* grown on the conductive CC could offer an efficient charge transfer channel and the fast release of bubbles during the OER/HER processes. The optimized 1 T-Co₄S₃-WS₂/CC catalyst promoted reaction kinetics and exhibited excellent OER and HER activities in alkaline solu-

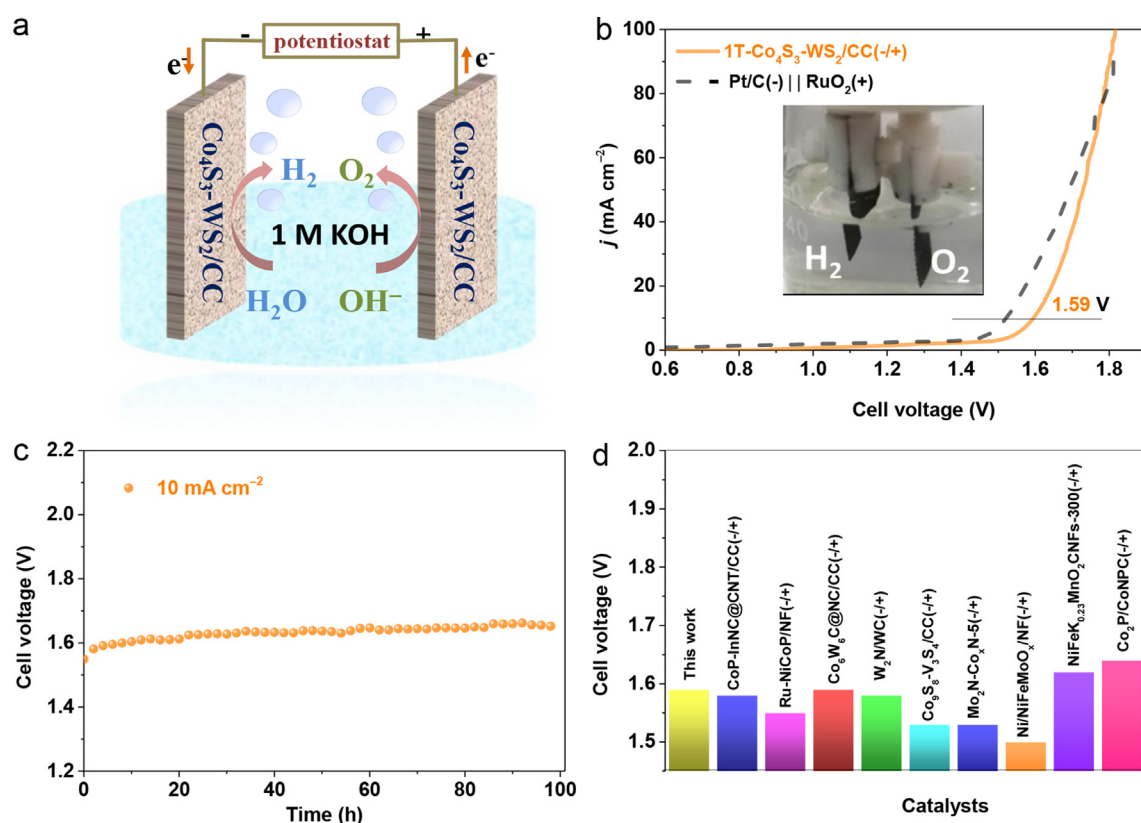


Fig. 6. (a) Schematic description of overall water splitting in the two-electrode system. (b) Polarization curves by the two-electrode design in 1.0 M KOH electrolyte (experimental phenomenon during catalyst stability test). (c) The chronoamperometric curve of 1 T-Co₄S₃-WS₂/CC(-/+) with the current density of 10 mA cm⁻² in the two-electrode system. (d) Comparison of the voltages at 10 mA cm⁻² with previously reported catalysts in 1.0 M KOH.

tion with low overpotentials of 278 and 75 mV at 10 mA cm⁻². Furthermore, the 1 T-Co₄S₃-WS₂/CC^(-/+) cell only requires the cell voltage of 1.59 V to achieve 10 mA cm⁻² with outstanding stability for 100 h. Overall, the synthetic strategy developed in this work could be extended to the design and synthesis of various low-cost, high-efficient WS₂-based electrocatalysts for water splitting. The process is scalable due to the simple synthesis, quantitative yield, and cheap reagents. It will stimulate a series of heterogeneous interfaces studies for electrochemical applications in future projects.

CRedit authorship contribution statement

Qimin Peng: Writing – original draft, Conceptualization. **Xue Shao:** Investigation, Data curation. **Chuan Hu:** Data curation. **Zuyang Luo:** Methodology. **Tayirjan Taylor Isimjan:** Writing – review & editing. **Zhifeng Dou:** Methodology, Writing – review & editing. **Ruobing Hou:** Supervision. **Xiulin Yang:** Supervision, Writing – review & editing.

Declaration of Competing Interest

The authors declare that they have no known competing financial interests or personal relationships that could have appeared to influence the work reported in this paper.

Acknowledgments

This work has been supported by the National Natural Science Foundation of China (no. 21965005), Natural Science Foundation of Guangxi Province (2018GXNSFAA294077, 2021GXNSFAA076001), Project of High-Level Talents of Guangxi (FKA18015, 2018ZD004), and Guangxi Technology Base and Talent Subject (GUIKE AD18126001, GUIKE AD20297039).

Appendix A. Supplementary material

Supplementary data to this article can be found online at <https://doi.org/10.1016/j.jcis.2022.02.031>.

References

- [1] L. Chai, Z. Hu, X. Wang, Y. Xu, L. Zhang, T.T. Li, Y. Hu, J. Qian, S. Huang, Stringing bimetallic metal-organic framework-derived cobalt phosphide composite for high-efficiency overall water splitting, *Adv. Sci.* 7 (2020) 1903195.
- [2] J. Chen, M. Gu, S. Liu, T. Sheng, X. Zhang, Iron doped in the subsurface of cus nanosheets by interionic redox: highly efficient electrocatalysts toward the oxygen evolution reaction, *ACS Appl. Mater. Interfaces* 13 (2021) 16210–16217.
- [3] L. Chen, H. Jang, M.G. Kim, Q. Qin, X. Liu, J. Cho, Fe, Al-co-doped NiSe₂ nanoparticles on reduced graphene oxide as an efficient bifunctional electrocatalyst for overall water splitting, *Nanoscale* 12 (25) (2020) 13680–13687.
- [4] J. Chen, B. Ren, H. Cui, C. Wang, Constructing pure phase tungsten-based bimetallic carbide nanosheet as an efficient bifunctional electrocatalyst for overall water splitting, *Small* 16 (2020) 1907556.
- [5] L. Chen, H. Jang, M.G. Kim, Q. Qin, X. Liu, J. Cho, Fe_xNi_y/CeO₂ loaded on N-doped nanocarbon as an advanced bifunctional electrocatalyst for the overall water splitting, *Inorg. Chem. Front.* 7 (2) (2020) 470–476.
- [6] H.-S. Hu, Y. Li, Y.-R. Shao, K.-X. Li, G. Deng, C.-B. Wang, Y.-Y. Feng, NiCoP nanorod arrays as high-performance bifunctional electrocatalyst for overall water splitting at high current densities, *J. Power Sources* 484 (2021) 229269.
- [7] P. Hou, D. Li, N. Yang, J. Wan, C. Zhang, X. Zhang, H. Jiang, Q. Zhang, L. Gu, D. Wang, Delicate control on the shell structure of hollow spheres enables tunable mass transport in water splitting, *Angew. Chem. Int. Ed.* 60 (13) (2021) 6926–6931.
- [8] J. He, X. Zhou, P. Xu, J. Sun, Promoting electrocatalytic water oxidation through tungsten-modulated oxygen vacancies on hierarchical FeNi-layered double hydroxide, *Nano Energy* 80 (2021) 105540.
- [9] L. Huang, D. Chen, G. Luo, Y.R. Lu, C. Chen, Y. Zou, C.L. Dong, Y. Li, S. Wang, Zirconium-regulation-induced bifunctionality in 3D cobalt-iron oxide nanosheets for overall water splitting, *Adv. Mater.* 31 (2019) 1901439.
- [10] N. Kornienko, N. Heidary, G. Cibin, E. Reisner, Catalysis by design: development of a bifunctional water splitting catalyst through an operando measurement directed optimization cycle, *Chem. Sci.* 9 (2018) 5322–5333.
- [11] S. Sun, X. Zhou, B. Cong, W. Hong, G. Chen, Tailoring the d-band centers endows (Ni_xFe_{1-x})₂P nanosheets with efficient oxygen evolution catalysis, *ACS Catal.* 10 (16) (2020) 9086–9097.
- [12] J. Zhang, R. Cui, C. Gao, L. Bian, Y. Pu, X. Zhu, X. Li, W. Huang, Cation-modulated HER and OER activities of hierarchical VOOH hollow architectures for high-efficiency and stable overall water splitting, *Small* 15 (2019) 1904688.
- [13] L. Yan, H. Wang, J. Shen, J. Ning, Y. Zhong, Y. Hu, Formation of mesoporous Co/CoS/Metal-N-C@S, N-codoped hairy carbon polyhedrons as an efficient trifunctional electrocatalyst for Zn-air batteries and water splitting, *Chem. Eng. J.* 403 (2021) 126385.
- [14] X. Wu, T. Zhang, J. Wei, P. Feng, X. Yan, Y.u. Tang, Facile synthesis of Co and Ce dual-doped Ni₃S₂ nanosheets on Ni foam for enhanced oxygen evolution reaction, *Nano Res.* 13 (8) (2020) 2130–2135.
- [15] H. Song, M. Wu, Z. Tang, J.S. Tse, B. Yang, S. Lu, Single atom ruthenium-doped CoP/CDs nanosheets via splicing of carbon-dots for robust hydrogen production, *Angew. Chem. Int. Ed.* 60 (13) (2021) 7234–7244.
- [16] Z. Zheng, L. Yu, M. Gao, X. Chen, W. Zhou, C. Ma, L. Wu, J. Zhu, X. Meng, J. Hu, Y. Tu, S. Wu, J. Mao, Z. Tian, D. Deng, Boosting hydrogen evolution on MoS₂ via co-confining selenium in surface and cobalt in inner layer, *Nat. Commun.* 11 (2020) 3315.
- [17] G. Zhou, X. Wu, M. Zhao, H. Pang, L. Xu, J. Yang, Y. Tang, Interfacial engineering-triggered bifunctionality of CoS₂/MoS₂ nanocubes/nanosheet arrays for high-efficiency overall water splitting, *ChemSusChem* 14 (2) (2021) 699–708.
- [18] B. Wang, H. Huang, T. Sun, P. Yan, T.T. Isimjan, J. Tian, X. Yang, Dissolution reconstruction of electron-transfer enhanced hierarchical NiS_x-MoO₂ nanosponges as a promising industrialized hydrogen evolution catalyst beyond Pt/C, *J. Colloid Interface Sci.* 567 (2020) 339–346.
- [19] H. Zhou, F. Yu, J. Sun, R. He, Y. Wang, C.F. Guo, F. Wang, Y. Lan, Z. Ren, S. Chen, Highly active and durable self-standing WS₂/graphene hybrid catalysts for the hydrogen evolution reaction, *J. Mater. Chem. A* 4 (24) (2016) 9472–9476.
- [20] X. Zhao, X. Ma, J. Sun, D. Li, X. Yang, Enhanced catalytic activities of surfactant-assisted exfoliated WS₂ nanodots for hydrogen evolution, *ACS Nano* 10 (2) (2016) 2159–2166.
- [21] W. Yang, S. Zhang, Q. Chen, C. Zhang, Y. Wei, H. Jiang, Y. Lin, M. Zhao, Q. He, X. Wang, Y. Du, L. Song, S. Yang, A. Nie, X. Zou, Y. Gong, Conversion of intercalated MoO₃ to multi-heteroatoms-doped MoS₂ with high hydrogen evolution activity, *Adv. Mater.* 32 (2020) 2001167.
- [22] K. Shiva, H.S.S. Ramakrishna Matte, H.B. Rajendra, A.J. Bhattacharyya, C.N.R. Rao, Employing synergistic interactions between few-layer WS₂ and reduced graphene oxide to improve lithium storage, cyclability and rate capability of Li-ion batteries, *Nano Energy* 2 (5) (2013) 787–793.
- [23] R.J. Toh, Z. Sofer, J. Luxa, D. Sedmidubský, M. Pumera, 3R phase of MoS₂ and WS₂ outperforms the corresponding 2H phase for hydrogen evolution, *Chem. Commun.* 53 (21) (2017) 3054–3057.
- [24] S. Peng, L. Li, J. Zhang, T.L. Tan, T. Zhang, D. Ji, X. Han, F. Cheng, S. Ramakrishna, Engineering Co₃S₈/WS₂ array films as bifunctional electrocatalysts for efficient water splitting, *J. Mater. Chem. A* 5 (44) (2017) 23361–23368.
- [25] D. Wang, Q. Li, C. Han, Z. Xing, X. Yang, When NiO@Ni Meets WS₂ nanosheet array: a highly efficient and ultrastable electrocatalyst for overall water splitting, *ACS Cent. Sci.* 4 (2018) 112–119.
- [26] M. Mojaddami, A. Simchi, Robust water splitting on staggered gap heterojunctions based on WO₃\WS₂-MoS₂ nanostructures, *Renewable Energy* 162 (2020) 504–512.
- [27] R. Li, B. Hu, T. Yu, H. Chen, Y. Wang, S. Song, Insights into correlation among surface-structure-activity of cobalt-derived pre-catalyst for oxygen evolution reaction, *Adv. Sci.* 7 (2020) 1902830.
- [28] J. Rong, J. Xu, F. Qiu, Y. Zhu, Y. Fang, J. Xu, T. Zhang, Sea urchin-like MOF-derived formation of porous Cu₃P@C as an efficient and stable electrocatalyst for oxygen evolution and hydrogen evolution reactions, *Adv. Mater.* 6 (2019) 1900502.
- [29] D.R. Paudel, U.N. Pan, T.I. Singh, C.C. Gudal, N.H. Kim, J.H. Lee, Fe and P doped 1T-phase enriched WS₂3D-dendritic nanostructures for efficient overall water splitting, *Appl. Catal. B: Environ.* 286 (2021) 119897.
- [30] S. Guo, Y. Li, C. Xue, Y. Sun, C. Wu, G. Shao, P. Zhang, Controllable construction of hierarchically CdIn₂S₄/CNFs/Co₄S₃ nanofiber networks towards photocatalytic hydrogen evolution, *Chem. Eng. J.* 419 (2021) 129213.
- [31] A. Wu, Y. Gu, B. Yang, H. Wu, H. Yan, Y. Jiao, D. Wang, C. Tian, H. Fu, Porous cobalt/tungsten nitride polyhedra as efficient bifunctional electrocatalysts for overall water splitting, *J. Mater. Chem. A* 8 (43) (2020) 22938–22946.
- [32] W. Han, Z. Liu, Y. Pan, G. Guo, J. Zou, Y. Xia, Z. Peng, W. Li, A. Dong, Designing champion nanostructures of tungsten dichalcogenides for electrocatalytic hydrogen evolution, *Adv. Mater.* 32 (2020) 2002584.
- [33] Y. Liu, X. Luo, C. Zhou, S. Du, D. Zhen, B. Chen, J. Li, Q. Wu, Y. Iru, D. Chen, A modulated electronic state strategy designed to integrate active HER and OER components as hybrid heterostructures for efficient overall water splitting, *Appl. Catal. B: Environ.* 260 (2020) 118197.
- [34] Z. Liu, N.a. Li, C. Su, H. Zhao, L. Xu, Z. Yin, J.u. Li, Y. Du, Colloidal synthesis of 1T' phase dominated WS₂ towards durable electrocatalysis, *Nano Energy* 50 (2018) 176–181.
- [35] B. Mahler, V. Hoepfner, K. Liao, G.A. Ozin, Colloidal synthesis of 1T-WS₂ and 2H-WS₂ nanosheets: applications for photocatalytic hydrogen evolution, *J. Am. Chem. Soc.* 136 (2014) 14121–14127.

- [36] Y. Yang, X. Shao, S. Zhou, P. Yan, T.T. Isimjan, X. Yang, Interfacial electronic coupling of NC@WO₃-W₂C decorated Ru clusters as a reversible catalyst toward electrocatalytic hydrogen oxidation and evolution reactions, *ChemSusChem* 14 (14) (2021) 2992–3000.
- [37] M.A. Ahsan, A.R. Puente Santiago, Y.u. Hong, N. Zhang, M. Cano, E. Rodriguez-Castellon, L. Echegoyen, S.T. Sreenivasan, J.C. Noveron, Tuning of trifunctional NiCu bimetallic nanoparticles confined in a porous carbon network with surface composition and local structural distortions for the electrocatalytic oxygen reduction, oxygen and hydrogen evolution reactions, *J. Am. Chem. Soc.* 142 (34) (2020) 14688–14701.
- [38] T.T. Debela, Y.R. Lim, H.W. Seo, I.S. Kwon, I.H. Kwak, J. Park, W.I. Cho, H.S. Kang, Two-dimensional WS₂@nitrogen-doped graphite for high-performance lithium ion batteries: experiments and molecular dynamics simulations, *ACS Appl. Mater. Interfaces* 10 (44) (2018) 37928–37936.
- [39] X. Ji, Y. Lin, J. Zeng, Z. Ren, Z. Lin, Y. Mu, Y. Qiu, J. Yu, Graphene/MoS₂/FeCoNi(OH)_x and graphene/MoS₂/FeCoNi_x multilayer-stacked vertical nanosheets on carbon fibers for highly efficient overall water splitting, *Nat. Commun.* 12 (2021) 1380.
- [40] C. Wu, J. Zhang, J. Guo, L. Sun, J. Ming, H. Dong, Y. Zhao, J. Tian, X. Yang, Ceria-induced strategy to tailor Pt atomic clusters on cobalt-nickel oxide and the synergetic effect for superior hydrogen generation, *ACS Sustain. Chem. Eng.* 6 (6) (2018) 7451–7457.
- [41] X. Shao, Y. Yang, Y.i. Liu, P. Yan, S. Zhou, T. Taylor Isimjan, X. Yang, Oxygen vacancy-rich N-doped carbon encapsulated BiOCl-CNTs heterostructures as robust electrocatalyst synergistically promote oxygen reduction and Zn-air batteries, *J. Colloid Interface Sci.* 607 (2022) 826–835.
- [42] D. Zhao, Z. Tang, W. Xu, Z. Wu, L.J. Ma, Z. Cui, C. Yang, L. Li, N, S-codoped CNTs supported Co₄S₃ nanoparticles prepared by using CdS nanorods as sulfur sources and hard templates: an efficient catalyst for reversible oxygen electrocatalysis, *J. Colloid Interface Sci.* 560 (2020) 186–197.
- [43] Y. Cheng, J. Gong, B.o. Cao, X. Xu, P. Jing, B. Liu, R. Gao, J. Zhang, An Ingenious strategy to integrate multiple electrocatalytically active components within a well-aligned nitrogen-doped carbon nanotube array electrode for electrocatalysis, *ACS Catal.* 11 (7) (2021) 3958–3974.
- [44] X.F. Lu, Y. Chen, S. Wang, S. Gao, X.W.D. Lou, Interfacing manganese oxide and cobalt in porous graphitic carbon polyhedrons boosts oxygen electrocatalysis for Zn-air batteries, *Adv. Mater.* 31 (2019) 1902339.
- [45] A. Han, X. Zhou, X. Wang, S. Liu, Q. Xiong, Q. Zhang, L. Gu, Z. Zhuang, W. Zhang, F. Li, D. Wang, L.J. Li, Y. Li, One-step synthesis of single-site vanadium substitution in 1T-WS₂ monolayers for enhanced hydrogen evolution catalysis, *Nat. Commun.* 12 (2021) 709.
- [46] S. Jiang, R. Zhang, H. Liu, Y. Rao, Y. Yu, S. Chen, Q. Yue, Y. Zhang, Y. Kang, Promoting formation of oxygen vacancies in two-dimensional cobalt-doped ceria nanosheets for efficient hydrogen evolution, *J. Am. Chem. Soc.* 142 (14) (2020) 6461–6466.
- [47] M. Wang, L.i. Zhang, M. Huang, Q. Zhang, X. Zhao, Y. He, S. Lin, J. Pan, H. Zhu, One-step synthesis of a hierarchical self-supported WS₂ film for efficient electrocatalytic hydrogen evolution, *J. Mater. Chem. A* 7 (39) (2019) 22405–22411.
- [48] Q.i. Wang, X. Huang, Z.L. Zhao, M. Wang, B. Xiang, J. Li, Z. Feng, H.u. Xu, M. Gu, Ultrahigh-loading of Ir single atoms on NiO matrix to dramatically enhance oxygen evolution reaction, *J. Am. Chem. Soc.* 142 (16) (2020) 7425–7433.
- [49] T. Zhao, X. Shen, Y. Wang, R.K. Hocking, Y. Li, C. Rong, K. Dastafkan, Z. Su, C. Zhao, In situ reconstruction of V-doped Ni 2 P pre-catalysts with tunable electronic structures for water oxidation, *Adv. Funct. Mater.* 31 (25) (2021) 2100614.
- [50] C.C.L. McCrory, S. Jung, J.C. Peters, T.F. Jaramillo, Benchmarking heterogeneous electrocatalysts for the oxygen evolution reaction, *J. Am. Chem. Soc.* 135 (45) (2013) 16977–16987.
- [51] J. Diao, Y. Qiu, S. Liu, W. Wang, K. Chen, H. Li, W. Yuan, Y. Qu, X. Guo, Interfacial engineering of W₂N/WC heterostructures derived from solid-state synthesis: a highly efficient trifunctional electrocatalyst for ORR, OER, and HER, *Adv. Mater.* 32 (2020) 1905679.
- [52] H. Duan, C. Wang, G. Li, H. Tan, W. Hu, L. Cai, W. Liu, N.a. Li, Q. Ji, Y. Wang, Y. Lu, W. Yan, F. Hu, W. Zhang, Z. Sun, Z. Qi, L.i. Song, S. Wei, Single-atom-layer catalysis in a MoS₂ monolayer activated by long-range ferromagnetism for the hydrogen evolution reaction: beyond single-atom catalysis, *Angew. Chem. Int. Ed.* 60 (13) (2021) 7251–7258.
- [53] Y. Yao, Y. Zhu, C. Pan, C. Wang, S. Hu, W. Xiao, X. Chi, Y. Fang, J.i. Yang, H. Deng, S. Xiao, J. Li, Z. Luo, Y. Guo, Interfacial sp C-O-Mo hybridization originated high-current density hydrogen evolution, *J. Am. Chem. Soc.* 143 (23) (2021) 8720–8730.
- [54] F. Li, G.F. Han, H.J. Noh, J.P. Jeon, I. Ahmad, S. Chen, C. Yang, Y. Bu, Z. Fu, Y. Lu, J. B. Baek, Balancing hydrogen adsorption/desorption by orbital modulation for efficient hydrogen evolution catalysis, *Nat. Commun.* 10 (2019) 4060.
- [55] Y. Yang, H. Fei, G. Ruan, Y. Li, J.M. Tour, Vertically aligned WS₂ nanosheets for water splitting, *Adv. Funct. Mater.* 25 (39) (2015) 6199–6204.
- [56] Q. Peng, Q. He, Y. Hu, T.T. Isimjan, R. Hou, X. Yang, Interface engineering of porous Fe₂P-WO_{2.92} catalyst with oxygen vacancies for highly active and stable large-current oxygen evolution and overall water splitting, *J. Energy Chem.* 65 (2022) 574–582.
- [57] Y. Ling, M. Li, K. Qu, Z. Yang, Electronically interacted Co₃O₄/WS₂ as superior oxygen electrode for rechargeable zinc-air batteries, *Chem. Commun.* 56 (96) (2020) 15193–15196.